PAPER

Check for updates

Short-range amorphous carbon nanosheets for oxygen reduction electrocatalysis†

Qingyu Li, [ID] Dingding Kong, Xinyi Zhao, Yezheng Cai, [ID]* Zhaoling Ma, [ID]*
Youguo Huang and Hongqiang Wang [ID]

Selectively creating active sites that can work well in different media as much as possible remains an open challenge for the widespread application of sustainable metal air batteries and fuel cells. Herein, short-range amorphous nitrogen-doped carbon nanosheets (NCS) coupled with partially graphitized porous carbon architecture were reported, and were prepared *via* flexible salt-assisted calcination strategy and followed by a simple cleaning process. The short-range amorphous structure not only significantly promotes the exposure of electrochemically active sites of carbon defects with less protonation in acidic medium, but also maintains the structural stability and electron conduction of the NCS. This unique structure endows the NCS (0.832 V) with efficient ORR electrocatalytic performance with a high half-wave potential ($E_{1/2}$) comparable to that of commercial Pt/C (0.837 V) in alkaline electrolyte and an impressive $E_{1/2}$ of 0.64 V in harsh acidic medium, making it outstanding among the reported analogous metal-free carbon electrocatalysts. In addition, the NCS manifests robust stability for ORR electrocatalysis with little change in the catalytic activity after accelerated stability tests. This work will provide a feasible inspiration to the construction of carbon nanomaterials with high active site density for efficient energy conversion-related electrochemical reactions.

1. Introduction

Promoting the development of renewable and clean energy conversion technologies, such as fuel cell and metal–air batteries, is highly desirable for relieving the global energy and environmental issues.[1–4] However, it remains arduously challenging because of the lack of efficient but cost-affordable electrode materials to accelerate the critical electrochemical reaction, known as the oxygen reduction reaction (ORR), for high energy conversion efficiency. Pt-Based materials still represent the best ORR catalysts, but the scarcity and high price have posed inevitable challenges for their commercialization.[5,6] Therefore, exploring noble metal-free ORR catalysts that can replace Pt, especially in an acidic electrolyte in view of the commercial success of the acidic proton exchange membrane, is of great significance for largely reducing the cost and further promoting the widespread application of energy conversion devices.[7]

So far, great progress has been made in precious metal-free ORR catalysts, among which non-metal heteroatom (N, S, P, B, *etc.*)-doped metal-free carbon materials are considered to be the promising alternatives to Pt-based materials. This is

Guangxi Key Laboratory of Low Carbon Energy Materials, School of Chemistry and Pharmaceutical Sciences, Guangxi Normal University, Guilin, China. E-mail: 18810629627@163.com; zhaolingma@163.com

because of their natural advantages such as wide raw material sources, abundant reserves, low price, and excellent stability in both alkaline and acidic medium.[8,9] In particular, N-doped carbon materials have attracted great attention due to the higher ORR catalytic activity compared to other heteroatom-doped counterparts, and the ease of production due to the similar atomic radius of C and N.[10] The impressive ORR activity is mainly due to the tuned electron cloud density and spin distribution of the original inert carbon materials caused by the introduction of N with higher electronegativity, thereby promoting the activation and decomposition of the oxygen molecule.[10] However, most N-doped carbon catalysts demonstrated excellent ORR catalytic performance only in an alkaline electrolyte, and unacceptably poor activity in an acid electrolyte. This can be attributed to the insufficient oxygen adsorption due to the existence of the pyridine nitrogen protonation and unbalanced hydrophilic/hydrophobic properties of pore structure, leading to a decreased density of effective active sites in acidic medium.[6,10,11] Hence, selectively exposing the active sites without protonation seems to be a feasible strategy for boosting the acidic ORR activity. Moreover, in addition to the nitrogen-containing moieties, carbon defects have demonstrated potential ORR catalytic capability in both alkaline and acidic environments.[12–14] For example, carbon nanotube (CNT) and graphene materials with high crystallinity and carbon defects show promising electrocatalysis for ORR.[15–17] However, the limited carbon defects at the corners and stacking phenomenon

hinder the exposure of electrocatalytic active sites, as well as the expression of catalytic activity. To overcome these issues, Shui and co-workers notably reported that zigzag-edged graphene nanoribbons coupled with rigid CNT backbones exhibited impressive ORR catalytic performance even in an actual proton exchange membrane duel cell test.[18] However, this reported acidic ORR activity desperately needs further improvement considering the low half-wave potential examined in half-cell measurements, which may be due to the insufficient active site density. Normally, the amounts of graphite carbon and carbon defect usually need to be well balanced to ensure electron conduction and active site density. Accordingly, exposing the catalytically active sites as much as possible, while maintaining good electronic conduction of the carbon materials, still represents an open challenge. In addition, the flexible and economically viable construction of efficient metal-free carbon-based electrocatalysts with simultaneously enhanced ORR activity in both alkaline and acidic medium is mandatory for further lowering the cost of electrocatalysts.

In view of these challenges, herein, we report on short-range amorphous carbon nanosheets coupled with partially graphitized carbon, which were synthesized *via* salt-assisted calcination process. We reveal that the unique short-range amorphous structure can endow the resultant N-doped carbon nanosheets (NCS) with rich defects acting as ORR active sites in alkaline and acidic media, and the partially graphitized nanosheet structure could maintain good electron transfer, therefore cooperatively improving the ORR electrocatalysis. The well-constructed NCS exhibited high ORR activity comparable to that of commercial Pt/C in alkaline electrolyte. Moreover, in acidic medium, the NCS displayed outstanding activity for ORR with a half-wave potential of 0.64 V and a diffusion current density of 4.5 mA cm^{-2}. In addition, no significant activity decay can be seen for NCS after the accelerated stability test. The difference of the catalytic active sites and catalytic kinetics of ORR between acid and alkaline electrolytes was also revealed for the rational design of electrocatalysts that can be adapted to a wide pH range.

2. Experimental part

2.1 Materials

Sodium chloride (NaCl), urea (CH_4N_2O), citric acid ($C_6H_8O_7$) and perchloric acid ($HClO_4$) were purchased from China Guangdong Xilong Chemical Co., Ltd. Absolute ethanol and potassium hydroxide (KOH) were provided by Aladdin. Nafion solution (5 wt%) was purchased from DuPont. All reagents in this work are A.R. grade and used without further treatment. The deionized water (18.2 MΩ cm) was homemade.

2.2 Synthesis of N-doped carbon nanosheets

Short-range amorphous carbon sheets coupled with graphitized carbon were synthesized *via* a facile strategy of NaCl-assisted high temperature calcination. First, 5.0 g NaCl, 3.0 g CH_4N_2O, and 4.0 g $C_6H_8O_7$ were well dispersed in 50 mL of deionized water under stirring for 2 h. Then, the above obtained dispersion was dried at 80 °C to obtain the catalyst precursor. Next, the dried catalyst precursor was annealed to 800 °C in a tubular furnace with Ar as a protective gas with a temperature heating rate of 5 °C min^{-1}, and maintained at this temperature for 2 h before naturally cooling to room temperature. Subsequently, the produced black powder was washed with deionized water to remove the NaCl template, filtered, and dried to obtain short-range N-doped carbon nanosheets, marked as NCS. To reveal the effect of the annealing temperature on the microstructure of the final samples, the catalyst precursor was also annealed at 600 °C and 1000 °C for 2 h, and the obtained porous bulk N-doped carbon samples were marked as PBNC-600 and PBNC-1000, respectively. The bulk N-doped carbon (BNC) was synthesized in a manner that was similar to NCS, except that no NaCl was added.

For the synthesis of PBNC-3/3 or PBNC-3/5, 5 g NaCl, 3 g $CO(NH_2)_2$, and 3 g or 5 g $C_6H_8O_7$ were mixed in 50 mL deionized water and stirred for 2 h. The subsequent processes were the same as that for the synthesis of NCS.

2.3 Structural characterization

X-ray diffraction (XRD) patterns were measured by X-ray diffractometer (Rigaku D/max 2500) using Cu Kα at a rate of 5° min^{-1} to analyze the crystal structure of the synthesized materials. Scanning electron microscope (SEM, Helios NanoLab 600i) and transmission electron microscope (TEM, JEM-2100f) were used to characterize the morphology of the materials. The surface element composition and valence states of the materials were determined by X-ray photoelectron spectroscopy (XPS, ESCALAB 250Xi). Microscopic Raman spectroscopy (Raman, DXR 2xi) was measured by a confocal laser Raman instrument under a 532 nm laser light source. The N_2 adsorption–desorption isotherms were measured by a physisorption analyzer specific surface area, and the pore size distribution were measured by Brunauer–Emmett–Teller (BET) analysis (Micromeritics, ASAP 2460).

2.4 Electrochemical measurements

Before the electrochemical performance evaluation, 4.0 mg catalyst was well dispersed into 1.0 mL of a mixed solvent composed of 990 μL of absolute ethanol and 10 μL of Nafion solution under ultrasonic treatment for 30 min. Subsequently, the rotating disk electrode (RDE), after polishing with 30 nm aluminum hydroxide slurry and cleaning in absolute ethanol, 10 μL of the above-mentioned catalyst dispersion was dropped on the polished RDE and dried in air. This catalyst-coated RDE was used as the working electrode during the electrochemical measurements.

Electrochemical measurements were carried out on a 760e electrochemical workstation (Shanghai Chenhua). The ORR catalytic performance was evaluated in a three-electrode system by using a graphite rod and AgCl electrode (saturated KCl) as the counter electrode and reference electrode, respectively, in 0.1 M KOH or 0.1 M $HClO_4$ electrolyte at room temperature.[13,19] Cyclic voltammetry (CV) curves were recorded in N_2 or O_2-saturated electrolyte at a scan rate of 50 mV s^{-1}, and the linear

scan voltammetry (LSV) curves were recorded in O_2-saturated electrolyte at a scan rate of 10 mV s^{-1} at different rotating speeds of 400–1600 rpm. The reported potential in this work was converted into a reversible hydrogen electrode (RHE) potential based on the equation of $E(RHE) = E(AgCl) + 0.197 V + 0.059 \times pH$. For a catalyst, the electron transfer number (n) for catalyzing ORR was obtained on the basis of the Koutecky–Levich (K–L) equation.[20]

$$1/j = 1/j_k + 1/j_l = 1/j_k + 1/(B\omega^{0.5}) \tag{1}$$

$$B = 0.62nFC_0D_0^{2/3}\nu^{-1/6} \tag{2}$$

where j, j_l and j_k are the measured current density, diffusion-limited current density and kinetic-limited current density, respectively; ω is the angular velocity; n and F are the required electron-transferred number and Faraday constant, respectively; C_0 and D_0 are the electron transfer concentration of oxygen in 0.1 M KOH and diffusion coefficient, respectively; and ν is the kinematic viscosity.

The rotating ring disk electrode (RRDE, the diameter is 5.6 mm) test was also carried out to reveal the catalytic kinetics. The n and H_2O_2 yield of the catalyst were further calculated according to the following equations:[20]

$$n = 4N \times I_d/(I_r + N \times I_d) \tag{3}$$

$$H_2O_2\% = 200 \times I_r/(I_r + N \times I_d) \tag{4}$$

where I_d, I_r, and N represent the disk current, ring current, and the collection efficiency, respectively.

3. Results and discussion

The N-doped carbon nanosheets (NCS) with short-range amorphous structure were synthesized *via* a facile strategy of NaCl-assisted high temperature calcination. First, urea and citric acid with a rational mass ratio were well mixed with the NaCl template at room temperature to obtain a U–C/NaCl complex. Then, the U–C/NaCl complex was annealed at 800 °C for the formation of the short-range amorphous NCS. The introduced NaCl crystals here can be used as a template and dispersant for the construction of porous and short-range carbon sheets due to the melting of NaCl at high temperature.

The low-resolution SEM images (Fig. S1† and 1A) of NCS show the porous carbon framework structure with some carbon sheets. Interestingly, the short-range and curved carbon nanosheets with nanoscale thickness can be observed from the high-resolution SEM image (Fig. 1B) of NCS. These short-range nanosheets coupled with carbon framework not only endow the CNS with rich active sites and fast mass transfer for facilitating electrocatalysis, but also good structure stability since the stacking of
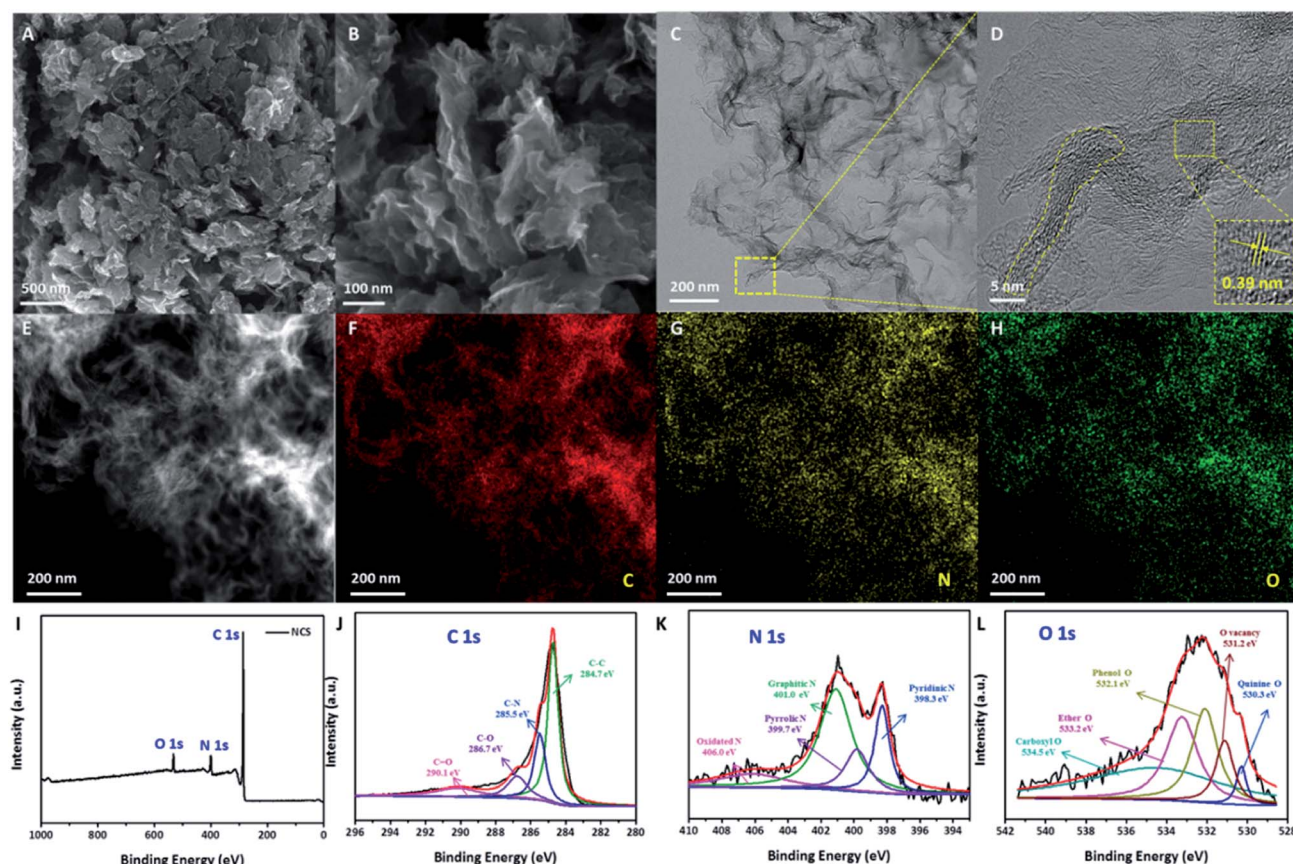

Fig. 1 (A–D) Low and high-resolution SEM (A and B) and TEM (C and D) images of NCS; (E–H) HAADF-STEM image and the corresponding elemental mapping images of NCS; (I–L) XPS survey scan (I) and high-resolution C 1s (J), N 1s (K), and O 1s (L) spectra of NCS.

the long-range nanosheets can be avoided. The carbon sheet structure of NCS was further confirmed by TEM (Fig. 1C) and high-resolution TEM (Fig. 1D) images, as evidenced from the existence of nearly transparent carbon sheets. Moreover, from a closer inspection of the high-resolution TEM image, one can also note that the carbon sheets consist of amorphous carbon along with some graphitic carbon, as confirmed from the presence of carbon lattice fringes in the middle area of the sheets (marked by yellow circles), suggesting the formation of short-range amorphous carbon sheets. In addition, the carbon lattice fringes exhibit an interplanar spacing of 0.39 nm that is larger than that of the kinetic diameter (3.46 Å) of the oxygen molecule, which is beneficial for the mass transfer of O_2 and therefore improved electrocatalytic kinetics. In previous work, the geometric size of amorphous carbon was normally larger than 100 nm and/or the amorphous carbon was generally randomly coupled with uneven graphitized carbon. However, in this work, the synthesized carbon consisted of short-range carbon sheets, which is composed of short-range amorphous coupled with partially graphitized carbon. So, compared with previous work, the unique feature of NCS as-prepared in this work is the short-range amorphous carbon nanosheets evenly coupled with partially graphitized carbon.[6,10,14] The nanosheet structure of NCS was further characterized by HADDF-STEM, as shown in Fig. 1E, showing the hierarchical feature along with the porous structure. The elemental mapping images (Fig. 1F–H) indicate the even distribution of C, N, and O across the NCS carbon nanosheets. The surface composition and valence states of the NCS were examined by XPS (Table S1† and Fig. 1I–L). The XPS survey scan (Fig. 1I) of NCS indicates the existence of C, N, and O. The high-resolution C 1s spectrum (Fig. 1J) shows four peaks

corresponding to the C–C, C–N, C–O, and C=O moieties.[21,22] In Fig. 1K, the high-resolution N 1s spectrum can be divided into four peaks of pyridinic N, pyrrolic N, graphitic N, and oxidized N.[23] The high-resolution O 1s spectrum (Fig. 1L) displays the presence of an oxygen vacancy, which is favorable for creating more active sites and enhancing the electronic conductivity, therefore benefiting the electrocatalysis.[24,25]

For comparison, BNC was synthesized similar to NCS except for the introduction of NaCl. The SEM image (Fig. S2A†) displays the formation of large bulk carbon, suggesting the key role of NaCl on the formation of the porous structure. Moreover, the U–C/NaCl complex was also annealed at 600 °C and 1000 °C. The resultant PBNC-600 and PBNC-1000 samples (Fig. S2B and C†) display big pores in the carbon bulks and collapsed carbon fragments, respectively, indicating that the carbon microstructure is highly dependent on the annealing temperature. The XPS survey scans, high-resolution XPS N 1s spectrum consisting of different N-contained moieties, and the compositions of BNC, PBNC-600, and PBNC-1000 are provided in Fig. S3 and Table S1.† It is worth noting that NCS has much lower N content than BNC and PBNC-600, which can be due to the larger exposure of the specific surface area of short-range carbon nanosheets. During the high temperature treatment, the surface N moieties tend to leave the carbon surface. The high-resolution N 1s spectra of BNC, PBNC-600, and PBNC-1000 in Fig. 2A indicate that NCS has a positive shift in the binding energy in comparison to BNC and PBNC-600. This suggested an electron transfer from nitrogen to carbon and decrease in the pyridinic N amount (Fig. S3†), which is beneficial for alleviating protonation.[10] The pyridinic N content of NCS, BNC and PBNC-600 were measured to be 17.59%, 19.20%, and 29.69%, respectively. However,
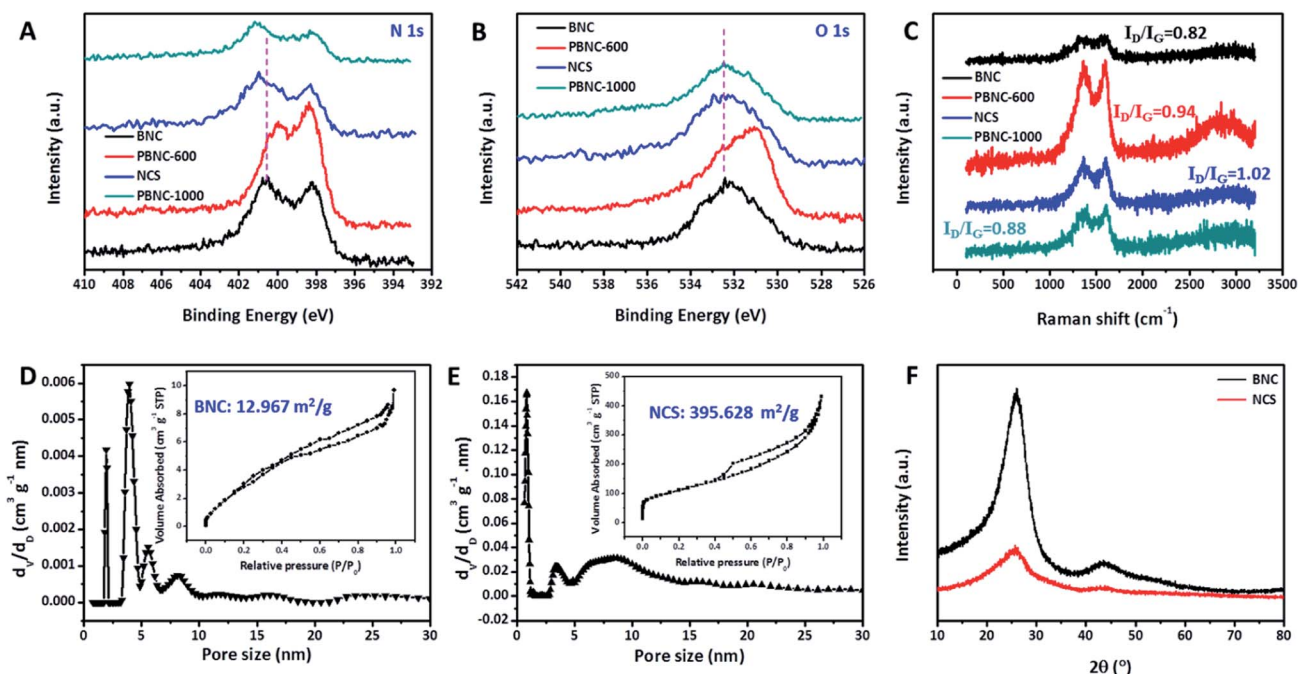

Fig. 2 High resolution (A) N 1s and (B) O 1s XPS spectra, (C) Raman spectra of BNC, PBNC-600, NCS, and PBNC-1000; (D and E) pore size distributions of BNC and NCS (the inset is the corresponding N_2 adsorption isotherm); (F) XRD patterns of BNC and NCS.

a further increase in the annealing temperature hardly changes the electronic properties of the N moieties, as confirmed by the similar binding energies of the N XPS spectra of NCS and PBNC-1000. Previous reports have demonstrated that the pyridinic N contributes to the ORR catalytic activity in both alkaline and acidic electrolytes.[10,11] However, the pyridinic N may be protonated in a low pH electrolyte due to the existence of basicity.[10] Therefore, a low pyridinic N content can decrease the unfavorable protonation, while increasing the ORR catalytic kinetics in acidic medium. Moreover, the high resolution O 1s spectra of these four samples compared in Fig. 2B show a phenomenon that is similar to the high resolution N 1s spectrum in Fig. 2A. The difference in the binding energy of the N 1s and O 1s spectra for these samples is related to the carbon structure features. A comparison of the Raman spectra of these samples in Fig. 2C show that the I_D/I_G value decreases in the order of NCS > PBNC-600 > PBNC-1000 > BNC, suggesting an increasing graphitization trend. Meanwhile, these different I_D/I_G values indicate that NCS possesses the highest amount of carbon defects, implying the largest active site density for efficiently catalyzing ORR.[26] Besides, the high I_D/I_G value of NCS also reveals the low crystallinity or partial amorphous structure of carbon architecture. N_2 adsorption measurements (Fig. 2D and E) reveal that NCS (395.628 m^2 g^{-1}) has a significantly large BET specific surface area than BNC (12.967 m^2 g^{-1}), suggesting the key role of the NaCl-assisted annealing process. Moreover, NCS consists of rich micropores and large mesopores, benefiting the accessibility of reactive substances and removal of product. To reveal the crystal structure of NCS, the XRD pattern was recorded and compared with that of BNC, as displayed in Fig. 2F. Obviously, BNC shows the two peaks of the

(002) and (100) graphitic carbon planes at 25.9° and 34.5°, respectively.[27] In contrast, only a peak with low intensity of the (200) plane of graphitic carbon can be seen, further implying the low crystallinity or partial amorphous structure, which is consistent with the TEM and Raman characterization results.

Motivated by the unique short-range amorphous nanosheets with rich defects and large specific surface area, we evaluated the ORR catalysis of NCS, as well as the control samples and commercial Pt/C catalyst. Compared to the CV curves (Fig. S4A and B†) recorded in N_2-saturated KOH solution, the CV curves recorded in O_2-saturated electrolyte manifest the obvious oxygen reduction peak with high current density at the cathodic scanning area, indicative of catalytic activity for ORR.[12,28] The current density of the material under N_2-saturated 0.1 M KOH solution is mainly related to the ECSA of the catalyst. NCS, showing the highest current density, can be due to the carbon sheet structure with large specific area. The LSV curves in Fig. 3A show that CNS (0.832 V) has a high half-wave potential ($E_{1/2}$) that is almost equivalent to that of commercial Pt/C (0.837 V). However, it is much higher than that of BNC (0.620 V) and many reported metal-free ORR electrocatalysts (Table S2†), suggesting efficient ORR electrocatalytic capability.[15] Meanwhile, NCS displays distinctly larger diffusion current density than BNC, implying a faster mass transfer benefiting from the short-range nanosheet structure. The lower Tafel slope of NCS in comparison to Pt/C further confirms the faster catalytic kinetics (Fig. 3B). Additionally, the kinetic current densities calculated at 0.85 V compared in Fig. 3C obviously demonstrate the sharp increase in the ORR activity of NCS compared to BNC. This impressive improvement can be ascribed to the effective exposure of the catalytically active sites of NCS, as confirmed by
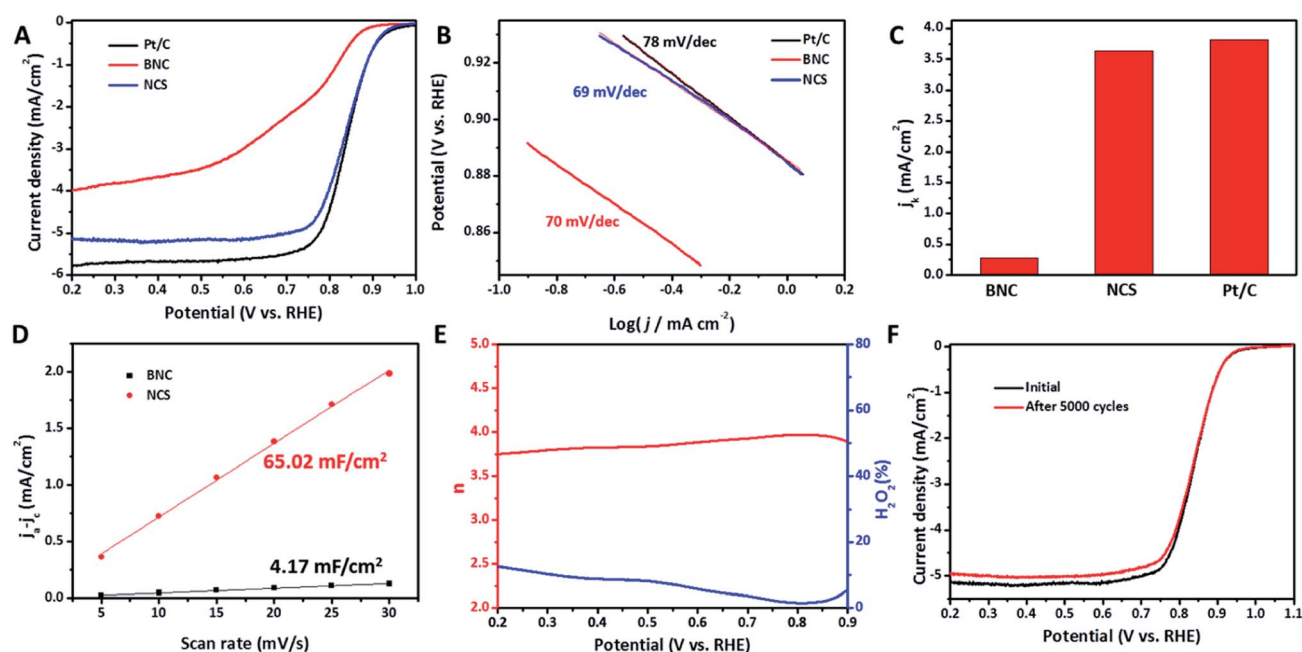

Fig. 3 Electrochemical performance in 0.1 M KOH solution. (A) LSV curves, (B) Tafel plots extracted from (A), and (C) the kinetic current densities (j_k) at 0.85 V of Pt/C, BNC, and NCS. (D) The linear relationship between capacitive (j_a-j_c) and CV scan rates of BNC and NCS. (E and F) Electron transfer number and H_2O_2 yield (E), and LSV curves before and after 5000 cycles (F) of NCS.

NCS presenting a large C_{dl} value, which is linearly related to the electrochemically active area over BNC (Fig. S4C, D† and 3D).[29] This inference was also well supported by the ORR catalytic performance results of PBNC-600 and PBNC-1000, as provided in Fig. S5,† revealing the central effect of the short-range nanosheets with rich defects. On the basis of the above ORR catalytic performance and structural characterizations, we note that NCS exhibits larger I_D/I_G value than that of BNC and PBNC-600 and BNC, which exhibited poor catalytic activity despite having high N content. Therefore, it can be concluded that it is the carbon defects acting as active sites contributing most to the impressive ORR activity of NCS. Furthermore, PBNC-3/3 and PBNC-3/5 were synthesized similar to NCS, except for the added amount of $C_6H_8O_7$ (3 g $C_6H_8O_7$ for the synthesis of PBNC-3/3 and 5 g for PBNC-3/5). Big pores in the carbon bulk without the formation of carbon sheets are presented, underlining the significance of the precursor composition on the microstructure of the final carbon sample (Fig. S6A and B†). Electrochemical performance results (Fig. S6C–H†) of PBNC-3/3 and PBNC-3/5 further highlight the promotion of the electrochemically active area of carbon defects for ORR. To understand the electrocatalytic kinetics of ORR on the as-synthesized electrocatalysts, the LVS curves of NCS at different rotating speeds were recorded and the linear fit K–L plots are displayed in Fig. S7.† The electron transfer numbers of ORR at different potentials indicate the highly efficient 4e⁻ electrocatalytic process.[30] In contrast, BNC, PBNC-600, and PBNC-1000 display a mixed pathway that consists of 2e⁻ and 4e⁻ (for BNC and PBNC-1000) or 2e⁻ (PBNC-600) processes for ORR (Fig. S8†). Moreover, the electrocatalytic mechanism was evaluated by conducting the RRDE test for NCS (Fig. S9†).[12] The calculated

electron transfer numbers are close to 4 and the H_2O_2 yields are low (<10%) in the potential range of 0.2–0.9 V, further demonstrating the approximate 4-electron catalytic process for ORR. In addition to the impressive catalytic activity, NCS presents robust electrocatalytic stability for ORR, as confirmed by the slight negative shift in the $E_{1/2}$ value even after an accelerated stability test of 5000-cycle CV scans (Fig. 3F).

Apart from the exciting ORR activity in alkaline medium, the unique structure of the short-range amorphous nanosheets also renders the NCS decent ORR electrocatalysis in a harsh acidic electrolyte of 0.1 M $HClO_4$.[28,31] The CV curve (Fig. 4A) of NCS recorded in O_2-saturated 0.1 M $HClO_4$ displays an additional reduction peak of the oxygen-containing species, suggesting the intrinsic catalytic activity toward ORR.[28] The redox peaks in Fig. 4A are a common phenomenon, and can be attributed to the oxidation and reduction of carbon and nitrogen-doped carbon moieties at >0.2 V vs. the standard hydrogen electrode.[3,6] The LSV curves (Fig. 4B) compared in Fig. 4A show that NCS has an encouraging ORR catalytic capability with an $E_{1/2}$ value of 0.64 V, along with a large diffusion current density. This $E_{1/2}$ value of NCS is outstanding or comparable among the reported metal-free or precious metal-free carbon materials, although it is still much lower than that (0.85 V) of commercial Pt/C (Table S3†). To understand the effect of the electrochemically active area for ORR electrocatalysis in an acidic electrolyte, the C_{dl} values of BNC and NCS were also measured by CV method (Fig. S10†). As in the alkaline electrolyte, CNS exhibits a significantly larger C_{dl} than BNC in acidic electrolyte, suggesting the distinct contribution of the short-range amorphous carbon nanosheets (Fig. 4C). Moreover, it should be noted that these C_{dl} values in acidic medium are much lower than those
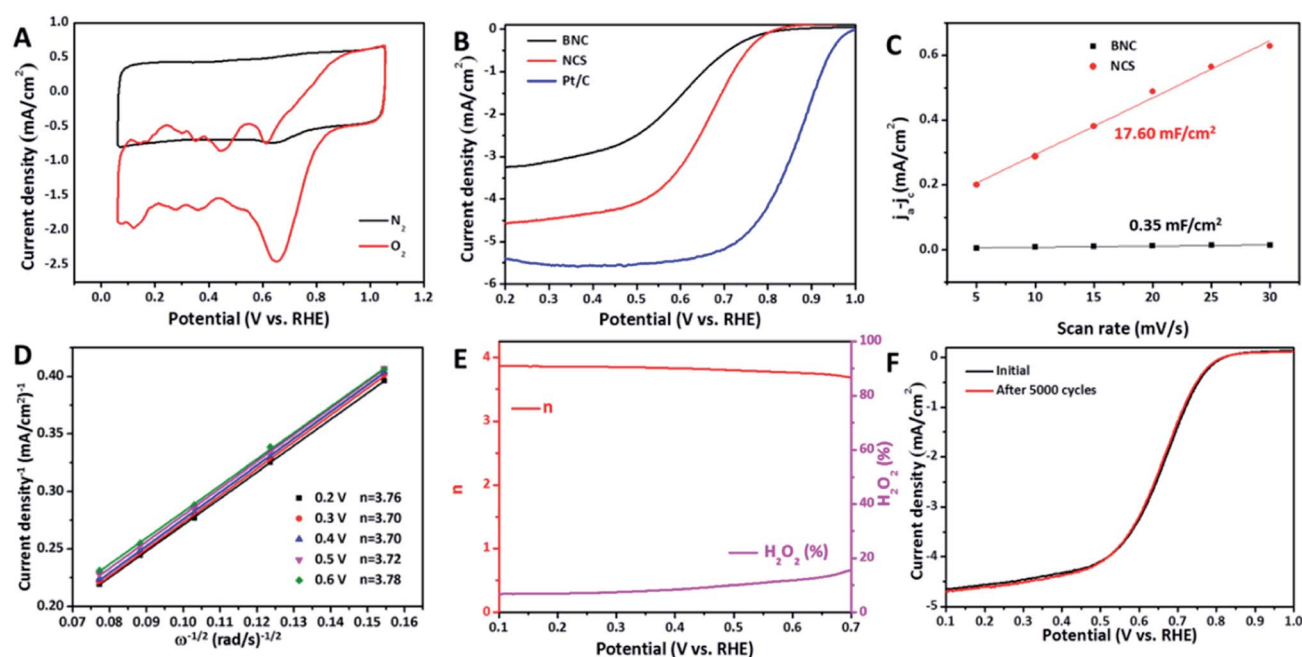

Fig. 4 (A) CV curves of NCS in N_2 or O_2-saturated 0.1 M $HClO_4$; (B) LSV curves of Pt/C, BNC, and NCS; (C) The linear relationship between capacitive (j_a–j_c) and CV scan rates of BNC and NCS; (D) Fitted K–L plots of NCS; (E and F) Electron transfer number and H_2O_2 yield (E), and LSV curves before and after 5000 cycles (F) of NCS.

examined in alkaline medium, confirming the different electrocatalytically active sites. In particular, for NCS, the acidic C_{dl} is a quarter of alkaline C_{dl}. Notably, BNC shows a sharp decrease in C_{dl} in acidic medium, which is one order of magnitude lower than the alkaline C_{dl}. These distinctly different decreases in C_{dl} could be caused by the different microstructure features of BNC and NCS. The rich defects in the short-range amorphous carbon nanosheets are electrochemically active in acidic medium with less protonation, accordingly endowing NCS with considerable acidic ORR activity.[32] However, some N-doping induced active sites may be inactive in acidic medium. Previous reports have confirmed that the active sites that can effectively catalyze ORR in an alkaline environment may be inactive in an acidic medium due to the protonation phenomenon and insufficient oxygen adsorption energy.[6,10,11] Therefore, the acidic activity for both BNC and NCS is lower than the alkaline activity for ORR. However, it should be noted that the well-constructed NCS possesses enhanced ORR catalytic capability over BNC in acidic medium, profiting from large density of carbon defects. Undeniably, there is a large gap of acidic ORR activity between the NCS and commercial Pt/C, which is the intrinsically low capability for oxygen adsorption, activation, and decomposition. Further enhancing the intrinsic activity of a single carbon active site in acidic medium is therefore more urgently indispensable, while creating high-density active sites.

The ORR pathway of NCS in acidic medium was also detected by recording the LSV curves at different rotating speeds of the working electrode (Fig. S11A†).[4,33] According to the obtained fitted K–L plots (Fig. 4D) on the basis of these LSV curves, the electron transfer number (n) of NCS between 0.2 V and 0.6 V was determined to be close to 4, suggesting a 4-electron pathway.[34] The RRDE measurement (Fig. S11B† and 4E) was performed as well to reveal the kinetics of ORR. The result further confirms the 4-electron process, and the high selectivity with low H_2O_2 yields of ORR on the NCS in the potential region of 0.1–0.7 V.[32,35] Apart from the decent activity, the NCS also displays reinforced catalytic stability for ORR with a slight shift (~3 mV) in the LSV curve even after the 5000-cycle accelerated stress test (Fig. 4F). In contrast, commercial Pt/C suffers a sharply negative shift (~34 mV) in $E_{1/2}$ in the same measurement (Fig. S12†).

4. Conclusion

In summary, our work presented a flexible and feasible strategy for improving ORR electrocatalysis by creating short-range amorphous carbon nanosheets with rich defects and partially graphitized carbon. This unique structure not only renders high density of active sites, which are considerably active in both alkaline and acidic medium, but also robust stability and good electronic transfer for the well-constructed NCS. The NCS exhibits high activity comparable to commercial Pt/C in alkaline medium and outstanding activity among the reported similar metal-free carbon catalysts in acidic medium, along with strong stability for electrocatalyzing ORR. Our findings will inspire more efforts to promoting carbon-based nanocatalysts by going from long-range nanosheets to short-range amorphous nanosheets for efficient energy conversion.

Conflicts of interest

There are no conflicts to declare.

Acknowledgements

References

1 Y. Li, Q. Li, H. Wang, L. Zhang, D. P. Wilkinson and J. Zhang, *Electrochem. Energy Rev.*, 2019, **2**, 518–538.

2 J. Lu, S. Yin and P. K. Shen, *Electrochem. Energy Rev.*, 2018, **2**, 105–127.

3 X. X. Wang, M. T. Swihart and G. Wu, *Nat. Catal.*, 2019, **2**, 578–589.

4 Z. Meng, S. Cai, R. Wang, H. Tang, S. Song and P. Tsiakaras, *Appl. Catal., B*, 2019, **244**, 120–127.

5 X. X. Wang, V. Prabhakaran, Y. He, Y. Shao and G. Wu, *Adv. Mater.*, 2019, **31**, 1805126–1805143.

6 Y. Shao, J. P. Dodelet, G. Wu and P. Zelenay, *Adv. Mater.*, 2019, **31**, 1807615–1807622.

7 U. Martinez, S. Komini Babu, E. F. Holby, H. T. Chung, X. Yin and P. Zelenay, *Adv. Mater.*, 2019, **31**, 1806545–1806564.

8 J. Quílez-Bermejo, E. Morallón and D. Cazorla-Amorós, *Carbon*, 2020, **165**, 434–454.

9 Y. Li, Y. Tong and F. Peng, *J. Energy Chem.*, 2020, **48**, 308–321.

10 L. Yang, J. Shui, L. Du, Y. Shao, J. Liu, L. Dai and Z. Hu, *Adv. Mater.*, 2019, **31**, 1804799–1804818.

11 S. K. Singh, K. Takeyasu and J. Nakamura, *Adv. Mater.*, 2019, **31**, 1804297–1804313.

12 L. Zong, W. Wu, S. Liu, H. Yin, Y. Chen, C. Liu, K. Fan, X. Zhao, X. Chen, F. Wang, Y. Yang, L. Wang and S. Feng, *Energy Storage Mater.*, 2020, **27**, 514–521.

13 R. Wu, X. Wan, J. Deng, X. Huang, S. Chen, W. Ding, L. Li, Q. Liao and Z. Wei, *Chem. Commun.*, 2019, **55**, 9023–9026.

14 H. Jiang, J. Gu, X. Zheng, M. Liu, X. Qiu, L. Wang, W. Li, Z. Chen, X. Ji and J. Li, *Energy Environ. Sci.*, 2019, **12**, 322–333.

15 N. Komba, Q. Wei, G. Zhang, F. Rosei and S. Sun, *Appl. Catal., B*, 2019, **243**, 373–380.

16 S.-B. Ren, X.-L. Chen, P.-X. Li, D.-Y. Hu, H.-L. Liu, W. Chen, W.-B. Xie, Y. Chen, X.-L. Yang, D.-M. Han, G.-H. Ning and X.-H. Xia, *J. Power Sources*, 2020, **461**, 228145–228150.

17 T. Gong, R. Qi, X. Liu, H. Li and Y. Zhang, *Nano-Micro Lett.*, 2019, **11**, 9–19.

18 L. Xue, Y. Li, X. Liu, Q. Liu, J. Shang, H. Duan, L. Dai and J. Shui, *Nat. Commun.*, 2018, **9**, 3819–3826.

19 G. Zhang, D. Sebastián, X. Zhang, Q. Wei, C. Lo Vecchio, J. Zhang, V. Baglio, W. Wang, S. Sun, A. S. Aricò and A. C. Tavares, *Adv. Energy Mater.*, 2020, **10**, 2000075–2000085.

20 X. Wan, X. Liu, Y. Li, R. Yu, L. Zheng, W. Yan, H. Wang, M. Xu and J. Shui, *Nat. Catal.*, 2019, **2**, 259–268.

21 K. P. Annamalai, X. Zheng, J. Gao, T. Chen and Y. Tao, *Carbon*, 2019, **144**, 185–192.

22 L. Chai, L. Zhang, X. Wang, L. Xu, C. Han, T.-T. Li, Y. Hu, J. Qian and S. Huang, *Carbon*, 2019, **146**, 248–256.

23 T. Najam, S. S. Ahmad Shah, H. Ali, Z. Song, H. Sun, Z. Peng and X. Cai, *Carbon*, 2020, **164**, 12–18.

24 D. Ji, L. Fan, L. Tao, Y. Sun, M. Li, G. Yang, T. Q. Tran, S. Ramakrishna and S. Guo, *Angew. Chem., Int. Ed.*, 2019, **58**, 13840–13844.

25 Y. Duan, Z.-Y. Yu, S.-J. Hu, X.-S. Zheng, C.-T. Zhang, H.-H. Ding, B.-C. Hu, Q.-Q. Fu, Z.-L. Yu, X. Zheng, J.-F. Zhu, M.-R. Gao and S.-H. Yu, *Angew. Chem., Int. Ed.*, 2019, **58**, 15772–15777.

26 Z. Zhang, H. Jin, J. Zhu, W. Li, C. Zhang, J. Zhao, F. Luo, Z. Sun and S. Mu, *Carbon*, 2020, **161**, 502–509.

27 H. Han, Y. Noh, Y. Kim, W. S. Jung, S. Park and W. B. Kim, *Nanoscale*, 2019, **11**, 2423–2433.

28 Z. Zhou, A. Chen, X. Fan, A. Kong and Y. Shan, *Appl. Surf. Sci.*, 2019, **464**, 380–387.

29 R. Zhao, Q. Li, Z. Chen, V. Jose, X. Jiang, G. Fu, J.-M. Lee and S. Huang, *Carbon*, 2020, **164**, 398–406.

30 Y. Zhao, X. Li, X. Jia and S. Gao, *Nano Energy*, 2019, **58**, 384–391.

31 M. Wang, H. Zhang, G. Thirunavukkarasu, I. Salam, J. R. Varcoe, P. Mardle, X. Li, S. Mu and S. Du, *ACS Energy Lett.*, 2019, 2104–2110.

32 S. Chen, N. Zhang, C. W. Narváez Villarrubia, X. Huang, L. Xie, X. Wang, X. Kong, H. Xu, G. Wu, J. Zeng and H.-L. Wang, *Nano Energy*, 2019, 104164–104171.

33 H. Wang, Y. Song, Y. Cao, H. Yu, H. Liang and F. Peng, *ACS Sustainable Chem. Eng.*, 2019, **7**, 10951–10961.

34 B. Li, S. P. Sasikala, D. H. Kim, J. Bak, I.-D. Kim, E. Cho and S. O. Kim, *Nano Energy*, 2019, **56**, 524–530.

35 M. Xiao, H. Zhang, Y. Chen, J. Zhu, L. Gao, Z. Jin, J. Ge, Z. Jiang, S. Chen, C. Liu and W. Xing, *Nano Energy*, 2018, **46**, 396–403.